# Supporting Information

## For

**Nickel foam and stainless steel mesh as electrocatalysts for hydrogen evolution reaction, oxygen evolution reaction and overall water splitting in alkaline media**

Xiaoyan Hu[a], Xuemei Tian[a], Ying-Wu Lin[b], and Zhonghua Wang*[a]

[a]Chemical Synthesis and Pollution Control Key Laboratory of Sichuan Province, College of Chemistry and Chemical Engineering, China West Normal University, Nanchong 637002, P.R. China

[b]School of Chemistry and Chemical Engineering, University of South China, Hengyang 421001, P. R. China

*Corresponding author.

Email: zhwangs@163.com, zhwangs@cwnu.edu.cn (Z. Wang).

Tel: (+86) 817-2568081, Fax: (+86) 817-2445233.

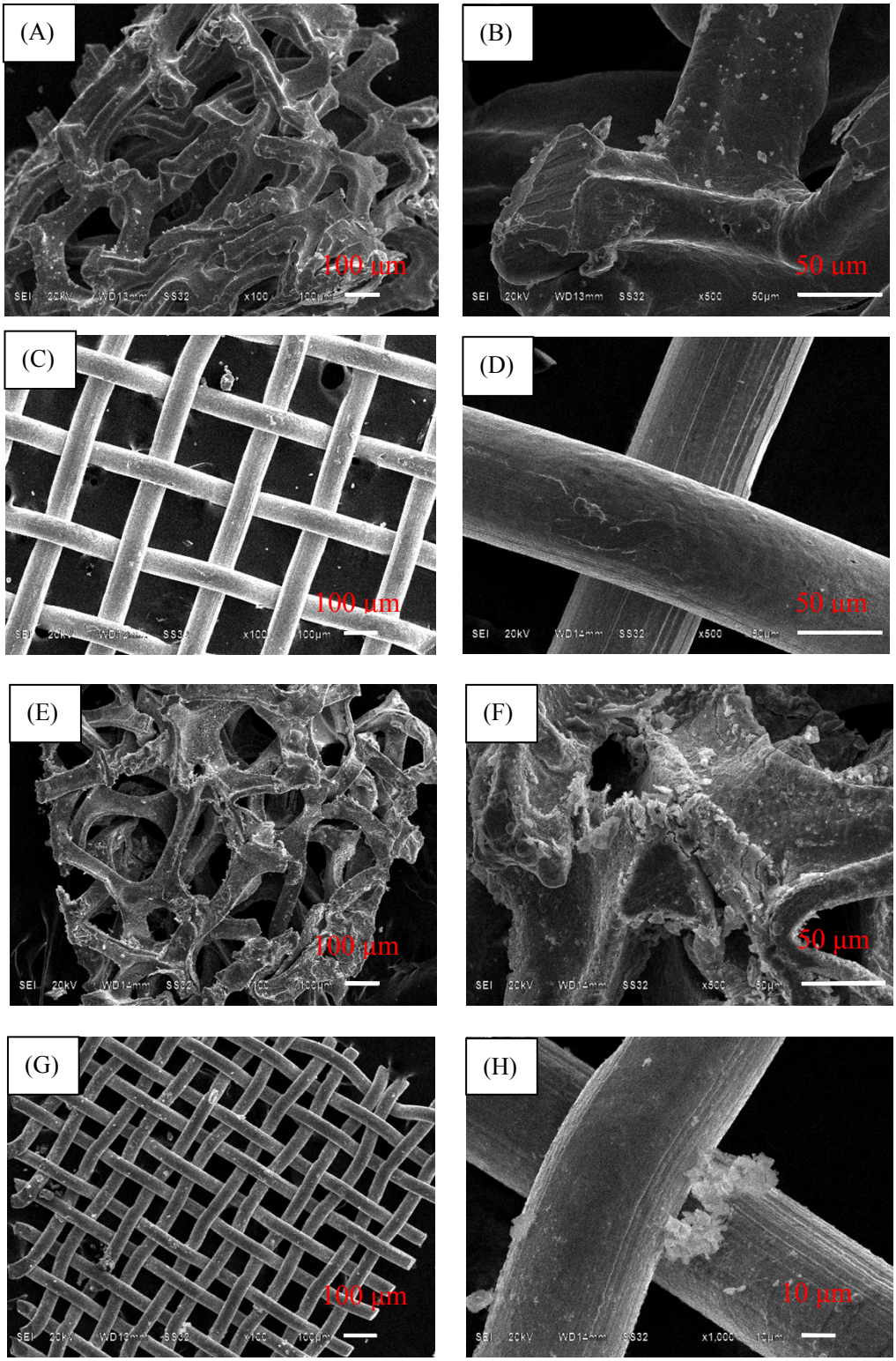


Fig. S1. The SEM images of Cu foam (A, B) and Ni mesh (C, D) before use. The SEM images of Ni foam (E, F) and SS mesh (G, H) after the stability test.

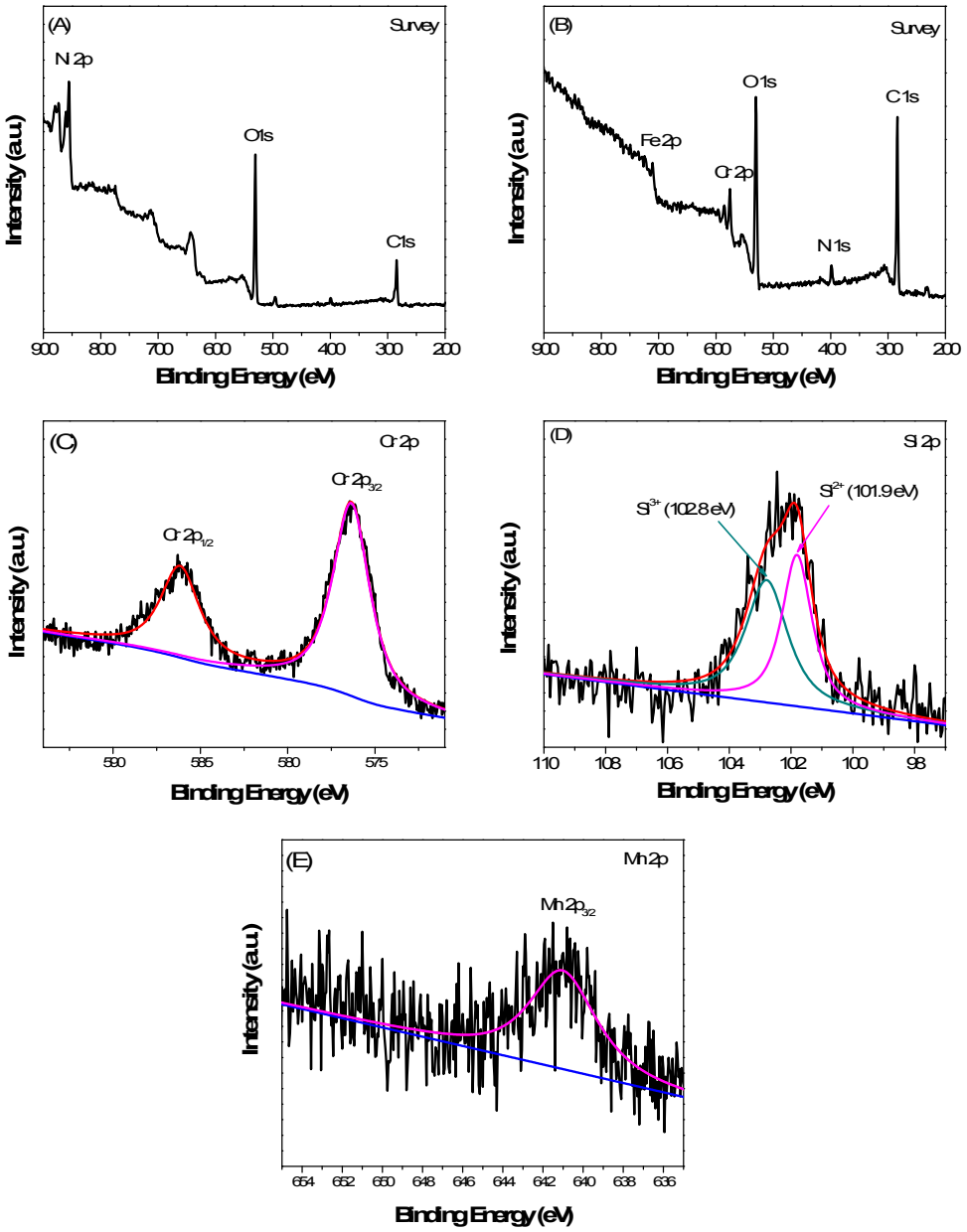


Fig. S2. The Survey XPS spectra of Ni foam (A) and SS mesh (B) before use; The high resolution XPS spectra of (C) Cr 2p and (D) Si 2p (E) Mn 2p of SS mesh before use.

In the Cr 2p region, the peaks at 586.3 and 576.4 eV correspond to the Cr 2p of $Cr^{3+}$ [1, 2]. The high-resolution Si 2p XPS spectra of SS mesh are shown in Fig. S2D, 102.8 eV was characteristics of $Si^{3+}$, while the peaks at 101.9 eV was characteristics of $Si^{2+}$ [3]. The spin-orbit components of the Mn $2p_{3/2}$ photoemission were located at 641.2 eV, which corresponds to MnO and $Mn_2O_3$ [4, 5].

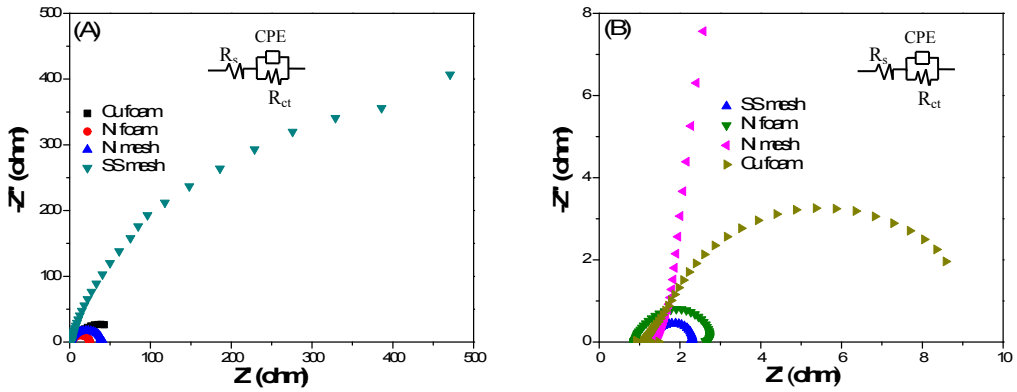


Fig. S3. Nyquist plots of EIS of samples with an amplitude of 5 mV (A) from $10^5$ Hz to 0.1 Hz (HER); (B) from 10 kHz to 0.01 Hz (OER).

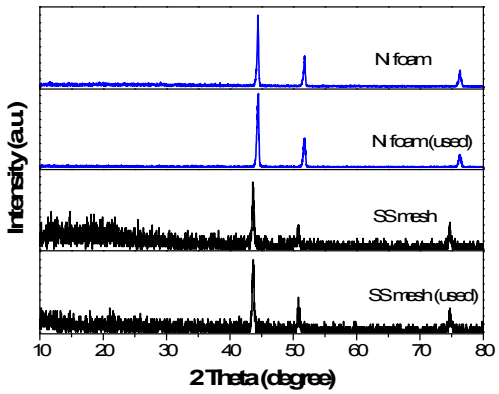


Fig. S4. Comparison of the XRD patterns of Ni foam and SS mesh before and after the stability test.

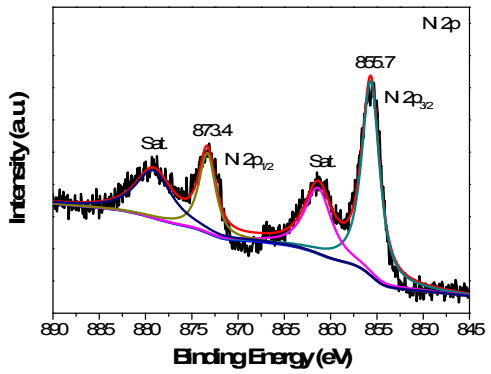


Fig. S5. The XPS spectra of Ni 2p of Ni foam after the stability test.

The XPS results of the Ni foam after the HER stability test are shown in the Fig. S5. The peaks at binding energies of 873.4 and 855.7 eV can be assigned to Ni $2p_{1/2}$ and Ni $2p_{3/2}$ of NiO, respectively [6]. The satellite peak at around 879.2 eV and 861.4 eV are two shake-up type peaks of nickel at the high binding energy side of the Ni $2p_{1/2}$ and Ni $2p_{3/2}$ edge [7]. Comparing the XPS data of the Ni 2p before (Fig. 3A) and after the stability test (Fig. S5), it can be seen that the peak at 852.1 eV disappeared after the electrocatalysis test, which shows the metallic nickel has been completely oxidized to NiO after the electrocatalysis test in 1 M KOH solution.

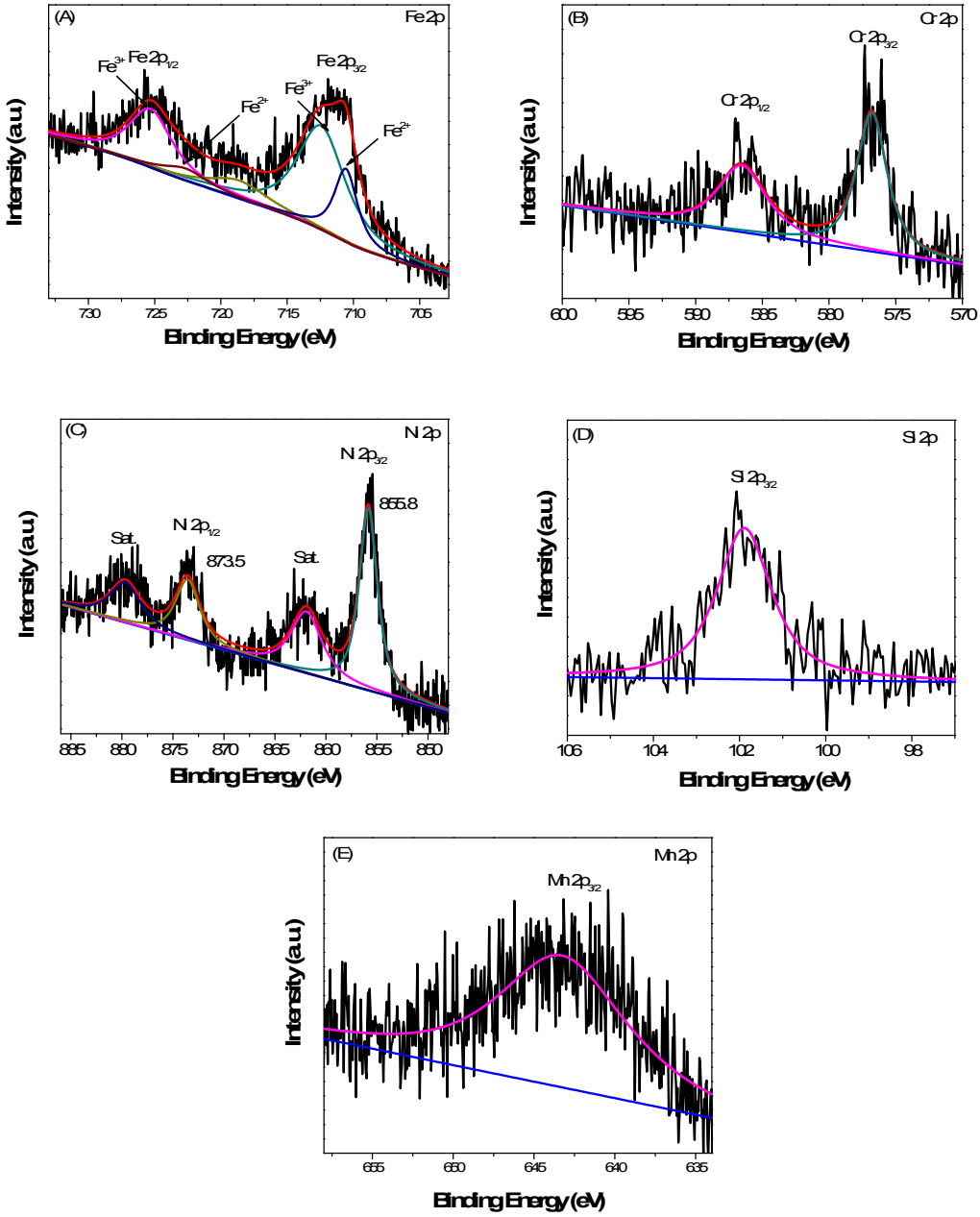


Fig. S6. The XPS spectra of Fe 2p (A), Cr 2p (B), Ni 2p (C), Si 2p (D) and Mn 2p (E) of SS mesh after the stability test.

The XPS results of the SS mesh after the OER stability test are shown in the Fig. S6. Fig. S6A shows the high resolution Fe 2p XPS of SS mesh after the stability test. The XPS spectrum of Fe 2p displays four peaks at 710.6, 712.5, 722.7 and 725.5 eV, which are attributed to the binding energy of Fe $2p_{3/2}$ and Fe $2p_{1/2}$, respectively. The peaks at 710.6 and 722.7 eV can be attributed to FeO [8], whereas the peaks at 712.5 and 725.5 eV can be assigned to $Fe_2O_3$ [8, 9]. Comparing the XPS data of the Fe 2p before and after the stability

test, it can be seen that the peak at 706.4 eV disappeared after the stability test, which shows the metal iron after the stability test has been completely oxidized. In addition, the XPS peak of $Fe^{2+}$ after the stability test decreased, and the peak area of $Fe^{3+}$ was relatively increased, which shows the part of the ferrous iron is converted into ferric iron, and Fe elements was existed as a mixture of FeO and $Fe_2O_3$ after the stability test. Fig. S6B shows the high resolution Cr 2p XPS spectrum of SS mesh after the stability test, the peaks at binding energies of 586.6 and 576.7 eV can be assigned to Cr 2p of $Cr^{3+}$ [1, 2]. Comparing the XPS data of the Cr 2p before and after the stability test, it can be seen that the peak of Cr element slightly weakens after the stability test. Fig. S6C shows the high resolution Ni 2p XPS of SS mesh after the stability test, the peaks at binding energies of 873.5 and 855.8 eV can be assigned to Ni $2p_{1/2}$ and Ni $2p_{3/2}$ of NiO, respectively [6]. The satellite peak at around 879.7 eV and 861.9 eV are two shake-up type peaks of nickel at the high binding energy side of the Ni $2p_{1/2}$ and Ni $2p_{3/2}$ edge [7], which shows that Ni elements of SS mesh was existed as NiO after the stability test. Fig. S6D shows the high resolution Si 2p XPS spectrum of SS mesh after the stability test, the peaks at 101.9 eV were characteristics of $Si^{2+}$ [3], which indicates that trivalent Si is completely converted into divalent Si after the stability test. Fig. S6E shows the high resolution Mn 2p XPS spectrum of SS mesh after the stability test, the peaks at binding energies of 643.3 eV can be assigned to $MnO_2$ [2], which indicates that trivalent Mn is converted into tetravalent Mn after the electrocatalysis test in 1 M KOH solution.

Table S1. The catalytic activity data of different catalysts for HER .

| Catalyst | η / (V vs RHE) (j = 10 mA $cm^{-2}$) | Ref |
|---|---|---|
| δ-$MnO_2$ | 80 mV | [10] |
| Fe/N-HCS-0.5-800 | 170 mV | [11] |
| $NOPHC_{10}$-900 | 290 mV | [12] |
| NiCoP | 118 mV | [13] |
| $Ni_3S_2$ | 200 mV | [14] |
| $W(S_{0.48}Se_{0.52})_2$ | 260 mV | [15] |
| $Ni_{0.9}Fe_{0.1}$/NC | 219 mV | [16] |
| $NiCo_2S_4$ | 210 mV | [17] |
| $Ni_3S_2$ | 223 mV | [18] |
| $Co_4Mo_2$@NC | 218 mV | [19] |
| $Mo(S_{0.49}Se_{0.51})_2$ | 271.3 mV | [20] |
| Ni foam | 217 mV | This work |

Table S2. The catalytic activity data of different catalysts for OER.

| Catalyst | η / (V vs RHE) (j = 10 mA $cm^{-2}$) | Ref |
|---|---|---|
| $Co_9S_8$ | 434 mV | [21] |
| $MnO_2$-$CoP_3$ | 288 mV | [22] |
| CuO-Co-0.2 | 394 mV | [23] |
| $Ni_3S_2$ | 187 mV | [24] |
| $Ni_3Se_2$ | 290 mV | [25] |
| NiCo-LDH | 271 mV | [26] |
| N-NiFe | 230 mV | [27] |
| $Ni_{2.53}$Ir NCs | 302 mV | [28] |
| CoS | 297 mV | [29] |
| CoP | 330 mV | [30] |
| SS mesh | 277 mV | This work |

Table S3. Water splitting cell voltage of different electrocatalysts.

| Catalyst | E (j = 10 mA $cm^{-2}$) | Ref |
|---|---|---|
| $NiFe/NiCo_2O_4/NF$ \|\| $NiFe/NiCo_2O_4/NF$ | 1.67 V | [31] |
| $Ni_5P_4$ \|\| $Ni_5P_4$ | 1.7 V | [32] |
| Er-doped CoP \|\| Er-doped CoP | 1.58 V | [33] |
| $Ni_{0.2}Co_{0.8}Se$ \|\| $Ni_{0.2}Co_{0.8}Se$ | 1.592 V | [34] |
| CoS-RGO \|\| CoS-RGO | 1.77 V | [35] |
| NESSP \|\| NESS | 1.74 V | [36] |
| SS scrubber \|\| SS scrubber | 1.98 V | [37] |
| $Co_1–Fe_1–B–P$ \|\| $Co_1–Fe_1–B–P$ | 1.68 V | [38] |
| ZIF-8-C6 \|\| ZIF-8-C4 | 1.82 V | [39] |
| $Co(OH)_2$@NCNTs@NF \|\| $Co(OH)_2$@NCNTs@NF | 1.72 V | [40] |
| Ni foam \|\| Stainless steel mesh | 1.74 V | This work |

## References


[1] S.-H. Zhang, M.-F. Wu, T.-T. Tang, Q.-J. Xing, C.-Q. Peng, F. Li, H. Liu, X.-B. Luo, J.-P. Zou, X.-B. Min, J.-M. Luo, Mechanism investigation of anoxic Cr(VI) removal by nano zero-valent iron based on XPS analysis in time scale, Chem. Eng. J., 335 (2018) 945-953.

[2] M.C. Biesinger, B.P. Payne, A.P. Grosvenor, L.W.M. Lau, A.R. Gerson, R.S.C. Smart, Resolving surface chemical states in XPS analysis of first row transition metals, oxides and hydroxides: Cr, Mn, Fe, Co and Ni, Appl. Surf. Sci., 257 (2011) 2717-2730.

[3] N. Zhou, Y. Wu, Q. Zhou, Y. Li, S. Liu, H. Zhang, Z. Zhou, M. Xia, Enhanced cycling performance and rate capacity of SiO anode material by compositing with monoclinic $TiO_2$ (B), Appl. Surf. Sci., 486 (2019) 292-302.

[4] P.G. Smirniotis, D.A. Pena, B.S. Uphade, Low-temperature selective catalytic reduction (SCR) of NO with $NH_3$ by using Mn,Cr,and Cu oxides supported on hombikat $TiO_2$, ChemBioChem, 32 (2010) 2479-2482.

[5] S. Swaminathan, C. Mallika, N.G. Krishna, C. Thinaharan, T. Jayakumar, U.K. Mudali, Evolution of surface chemistry and morphology of oxide scale formed during initial stage oxidation of modified 9Cr–1Mo steel, Corros. Sci., 79 (2014) 59-68.

[6] J. Landon, E. Demeter, N. İnoğlu, C. Keturakis, I.E. Wachs, R. Vasić, A.I. Frenkel, J.R. Kitchin,

Spectroscopic characterization of mixed Fe–Ni oxide electrocatalysts for the oxygen evolution reaction in alkaline electrolytes, ACS Catal., 2 (2012) 1793-1801.

[7] C. Jin, F. Lu, X. Cao, Z. Yang, R. Yang, Facile synthesis and excellent electrochemical properties of $NiCo_2O_4$ spinel nanowire arrays as a bifunctional catalyst for the oxygen reduction and evolution reaction, J. Mater. Chem. A, 1 (2013) 12170-12177.

[8] H. Xing, Z. Liu, L. Lin, L. Wang, D. Tan, Y. Gan, X. Ji, G. Xu, Excellent microwave absorption properties of Fe ion-doped $SnO_2$/multi-walled carbon nanotube composites, RSC Adv., 6 (2016) 41656-41664.

[9] H. Gu, Y. Jiang, M. Yan, Defect-induced room temperature ferromagnetism in Fe and Na co-doped ZnO nanoparticles, J. Alloys Compd., 521 (2012) 90-94.

[10] H. Begum, M.S. Ahmed, S. Jeon, δ-$MnO_2$ nanoflowers on sulfonated graphene sheets for stable oxygen reduction and hydrogen evolution reaction, Electrochim. Acta, 296 (2019) 235-242.

[11] K. Song, B. Shi, D. Song, Q. Zhang, X. He, Z. Dou, X. Hu, L. Cui, Tunable engineering hollow carbon nanomaterial served as an excellent catalyst for oxygen reduction reaction and hydrogen evolution reaction, J. Colloid Interface Sci., 544 (2019) 178-187.

[12] S. Huang, Y. Meng, Y. Cao, S. He, X. Li, S. Tong, M. Wu, N-, O- and P-doped hollow carbons: metal-free bifunctional electrocatalysts for hydrogen evolution and oxygen reduction reactions, Appl. Catal., B, 248 (2019) 239-248.

[13] T. Liu, X. Yan, P. Xi, J. Chen, D. Qin, D. Shan, S. Devaramani, X. Lu, Nickel–cobalt phosphide nanowires supported on Ni foam as a highly efficient catalyst for electrochemical hydrogen evolution reaction, Int. J. Hydrogen Energy, 42 (2017) 14124-14132.

[14] C. Ouyang, X. Wang, C. Wang, X. Zhang, J. Wu, Z. Ma, S. Dou, S. Wang, Hierarchically porous $Ni_3S_2$ nanorod array foam as highly efficient electrocatalyst for hydrogen evolution reaction and oxygen evolution reaction, Electrochim. Acta, 174 (2015) 297-301.

[15] K. Xu, F. Wang, Z. Wang, X. Zhan, Q. Wang, Z. Cheng, M. Safdar, J. He, Component-controllable $WS_{(2(1-x))}Se_{(2x)}$ nanotubes for efficient hydrogen evolution reaction, ACS nano, 8 (2014) 8468-8476.

[16] X. Zhang, H. Xu, X. Li, Y. Li, T. Yang, Y. Liang, Facile synthesis of nickel–iron/nanocarbon hybrids as advanced electrocatalysts for efficient water splitting, ACS Catal., 6 (2015) 580-588.

[17] A. Sivanantham, P. Ganesan, S. Shanmugam, Hierarchical $NiCo_2S_4$ nanowire arrays supported on

Ni foam: an efficient and durable bifunctional electrocatalyst for oxygen and hydrogen evolution reactions, Adv. Funct. Mater., 26 (2016) 4661-4672.

[18] L.L. Feng, G. Yu, Y. Wu, G.D. Li, H. Li, Y. Sun, T. Asefa, W. Chen, X. Zou, High-index faceted $Ni_3S_2$ nanosheet arrays as highly active and ultrastable electrocatalysts for water splitting, J. Am. Chem. Soc., 137 (2015) 14023-14026.

[19] J. Jiang, Q. Liu, C. Zeng, L. Ai, Cobalt/molybdenum carbide@N-doped carbon as bifunctional electrocatalysts for hydrogen and oxygen evolution reactions, J. Mater. Chem. A, 5 (2017) 16929-16935.

[20] B. Xia, L. An, D. Gao, S. Shi, P. Xi, D. Xue, Hierarchical ultrathin $Mo(S_xSe_{1-x})_2$nanosheets with tunable ferromagnetism and efficient hydrogen evolution reaction activity: towards defect site effect, CrystEngComm, 17 (2015) 6420-6425.

[21] L. Li, L. Song, H. Guo, W. Xia, C. Jiang, B. Gao, C. Wu, T. Wang, J. He, N-Doped porous carbon nanosheets decorated with graphitized carbon layer encapsulated $Co_9S_8$ nanoparticles: an efficient bifunctional electrocatalyst for the OER and ORR, Nanoscale, 11 (2019) 901-907.

[22] X. Xiong, Y. Ji, M. Xie, C. You, L. Yang, Z. Liu, A.M. Asiri, X. Sun, $MnO_2$-$CoP_3$ nanowires array: an efficient electrocatalyst for alkaline oxygen evolution reaction with enhanced activity, Electrochem. Commun., 86 (2018) 161-165.

[23] H. Xu, W. Liu, Y. Zhao, D. Wang, J. Zhao, Ammonia-induced synergistic construction of $Co_3O_4$@CuO microsheets: an efficient electrocatalyst for oxygen evolution reaction, J. Colloid Interface Sci., 540 (2019) 585-592.

[24] W. Zhou, X.J. Wu, X. Cao, X. Huang, C. Tan, J. Tian, H. Liu, J. Wang, H. Zhang, $Ni_3S_2$ nanorods/Ni foam composite electrode with low overpotential for electrocatalytic oxygen evolution, Energy Environ. Sci., 6 (2013) 2921-2924.

[25] A. Swesi, J. Masud, M. Nath, Nickel selenide as high-efficiency catalyst for oxygen evolution reaction, Energy Environ. Sci., 9 (2016) 1771-1782.

[26] W. Liu, J. Bao, M. Guan, Y. Zhao, J. Lian, J. Qiu, L. Xu, Y. Huang, J. Qian, H. Li, Nickel-cobalt-layered double hydroxide nanosheet arrays on Ni foam as a bifunctional electrocatalyst for overall water splitting, Dalton Trans., 46 (2017) 8372-8376.

[27] S. Chen, J. Duan, P. Bian, Y. Tang, R. Zheng, S.Z. Qiao, Three‐dimensional smart catalyst electrode for oxygen evolution reaction, Adv. Energy Mater., 5 (2015)

https://doi.org/10.1002/aenm.201500936.

[28] C. Wang, Y. Sui, M. Xu, C. Liu, G. Xiao, B. Zou, Synthesis of Ni-Ir nanocages with improved electrocatalytic performance for the oxygen evolution reaction, ACS Sustainable Chem. Eng., 5 (2017) 9787-9792.

[29] P. Guo, Y.X. Wu, W.M. Lau, H. Liu, L.M. Liu, CoS nanosheet arrays grown on nickel foam as an excellent OER catalyst, J. Alloys Compd., 723 (2017) 772-778.

[30] C.C. Hou, S. Cao, W.F. Fu, Y. Chen, Ultrafine CoP nanoparticles supported on carbon nanotubes as highly active electrocatalyst for both oxygen and hydrogen evolution in basic media, ACS Appl. Mater. Interfaces, 7 (2015) 28412-28419.

[31] C. Xiao, Y. Li, X. Lu, C. Zhao, Bifunctional Porous NiFe/$NiCo_2O_4$/Ni foam electrodes with triple hierarchy and double synergies for efficient whole cell water splitting, Adv. Funct. Mater., 26 (2016) 3515-3523.

[32] M. Ledendecker, C.S. Krick, C. Papp, H.P. Steinrück, M. Antonietti, M. Shalom, The synthesis of nanostructured $Ni_5P_4$ films and their use as a non-noble bifunctional electrocatalyst for full water splitting, Angew. Chem., 54 (2015) 12361-12365.

[33] G. Zhang, B. Wang, J. Bi, D. Fang, S. Yang, Constructing ultrathin CoP nanomeshes by Er-doping for highly efficient bifunctional electrocatalysts for overall water splitting, J. Mater. Chem. A, 7 (2019) 5769-5778.

[34] Z. Qian, Y. Chen, Z. Tang, Z. Liu, X. Wang, Y. Tian, W. Gao, Hollow nanocages of $Ni_xCo_{1-x}Se$ for efficient zinc–air batteries and overall water splitting, Nano-Micro Lett., 11 (2019) https://doi.org/10.1007/s40820-40019-40258-40820.

[35] Y. Chen, S. Xu, S. Zhu, R.J. Jacob, G. Pastel, Y. Wang, Y. Li, J. Dai, F. Chen, H. Xie, B. Liu, Y. Liu, L.G. Salamanca-Riba, M.R. Zachariah, T. Li, L. Hu, Millisecond synthesis of CoS nanoparticles for highly efficient overall water splitting, Nano Res., (2019) https://doi.org/10.1007/s12274-12019-12304-12270.

[36] M.S. Balogun, W. Qiu, Y. Huang, H. Yang, R. Xu, W. Zhao, G.R. Li, H. Ji, Y. Tong, Cost-effective alkaline water electrolysis based on nitrogen- and phosphorus-doped self-supportive electrocatalysts, Adv. Mater., 29 (2017) https://doi.org/10.1002/adma.201702095.

[37] S. Anantharaj, S. Chatterjee, T.S. Amarnath, E. Subhashini, D.K. Pattanayak, S. Kundu, Stainless steel scrubber: a cost efficient catalytic electrode for full water splitting in alkaline medium, ACS

Sustainable Chem. Eng., 6 (2018) 2498-2509.

[38] Z. Wu, D. Nie, M. Song, T. Jiao, G. Fu, X. Liu, Facile synthesis of Co-Fe-B-P nanochains as an efficient bifunctional electrocatalyst for overall water-splitting, Nanoscale, 11 (2019) 7506-7512.

[39] Y. Lei, L. Wei, S. Zhai, Y. Wang, C. Yuan, Metal-free bifunctional carbon electrocatalysts derived from zeolitic imidazolate framework for efficient water splitting, Mater. Chem. Front., 2 (2018) 102-111.

[40] P. Guo, J. Wu, X.-B. Li, J. Luo, W.-M. Lau, H. Liu, X.-L. Sun, L.-M. Liu, A highly stable bifunctional catalyst based on 3D $Co(OH)_2$@NCNTs@NF towards overall water-splitting, Nano Energy, 47 (2018) 96-104.